Monthly Notices of the ROYAL ASTRONOMICAL SOCIETY

MNRAS **543,** 1435–1446 (2025) https://doi.org/10.1093/mnras/staf1563
Advance Access publication 2025 September 16

ExoMol photodissociation cross-sections – IV. Photodissociation rates of the CH radical

Andrei Sokolov, Ryan P. Brady, Sergei N. Yurchenko and Jonathan Tennyson ★
Department of Physics and Astronomy, University College London, Gower St, London WC1E 6BT, UK

Accepted 2025 September 12. Received 2025 September 11; in original form 2025 August 6

ABSTRACT

Photodissociation cross-sections are computed as a function of temperature for the methylidyne radical, CH. The model explicitly considers the lowest 13 electronic states of CH and are topped up at short-wavelengths using available results. The effects of predissociation due to curve crossing and tunnelling through a centrifugal barrier are both explicitly considered, alongside direct photodissociation. Photodissociation rates of CH in standard astronomical radiation fields are large but found to show only minor dependence on the temperature of the CH, in contrast to previous studies on diatomic hydrides. The SBYT cross-sections are made available via the ExoPhoto data base www.exomol.com/ExoPhoto.

Key words: molecular data – molecular processes – exoplanets – stars: carbon – photodissociation region (PDR) – ultraviolet: general.

1 INTRODUCTION

In ultraviolet (UV)-rich stellar fields, photochemical processes have a strong influence on the composition and dynamics of molecular clouds, stellar, and planetary atmospheres. The development of reliable models of such environments to describe their chemistry, atmospheric conditions, as well as the interpretation of high-resolution spectroscopic observations of these objects relies on the availability of molecular photodissociation and photoionization data. A major source of these data has been the Leiden database (Heays, Bosman & van Dishoeck 2017; Hrodmarsson & Van Dishoeck 2023), where wavelength-dependent cross-sections for over a 100 atomic and molecular species are tabulated, along with the respective photodissociation and -ionization rates when these atoms and molecules are subject to various radiation fields. All of these theoretical data are provided for 0 K, where only the ground vibronic level is considered to be populated, and the cross-sections are not rotationally resolved. While sufficient for describing cold objects, such as the interstellar medium, for other astronomical objects at elevated temperatures the effect of lower state population should lead to changes in cross-sections and rates. In this work, we are using the recent methodology developed in ExoMol (Pezzella, Yurchenko & Tennyson 2021) and a new set of electronic structure data (Hou & Liu 2024) to calculate temperature-dependent photodissociation cross-sections for CH and its rates in several radiation fields.

The methylidyne radical, CH, is one of the most studied molecular species in astrophysics and has been observed in a variety of astronomical objects, including the Sun (Mélen et al. 1989; Grevesse et al. 1991), cool stars (Ridgway et al. 1984), comets (Womack, Lutz & Wagner 1994), interstellar medium (Lien 1984; Stacey, Lugten & Genzel 1987), and planetary nebulae (Liu et al. 1997). Its spectra are present in some of the oxygen-rich stars, most of the cool carbon-rich stars, and various spectral features of CH are used in classification of carbon giants (Lambert et al. 1986; Jørgensen et al. 1996). Its other uses involve studies of hydrocarbon flames (Rensberger, Dyer & Copeland 1988; Versailles et al. 2016) and testing the variations of the fundamental constants based on certain microwave transitions that can be measured with extremely high accuracy (De Nijs, Ubachs & Bethlem 2012; Truppe et al. 2014). The extensive literature on spectroscopic measurements of CH is collected and summarized by Civiš et al. (2023) and Furtenbacher et al. (2022).

As for the photodissociation cross-section data of CH, two main theoretical data sources exist. The first is the work of van Dishoeck (1987) used in the Leiden data base, which employs an extensive multistate model of CH to obtain the cross-sections over a wide spectral range, but only for low temperature. Predissociation processes are approximated using the Fermi's golden rule, and direct photoabsorption is obtained by solving the scattering problem. The other source is Kurucz, Van Dishoeck & Tarafdar (1987), where partially rotationally resolved continuum absorption cross-sections have been generated for hot conditions $T = 1000$–9000 K. Predissociation effects were not considered there. The data by Kurucz et al. (1987) have been recently used in Popa et al. (2023) to estimate the magnitude of non-local thermodynamic equilibrium (LTE) effects in cool stellar atmospheres of red giants, and the departures from equilibrium have been found to be non-negligible due to strong and low-threshold photodissociation. To facilitate such studies of hot carbon-rich systems, this paper aims to provide temperature-dependent photodissociation cross-sections.

★ E-mail: j.tennyson@ucl.ac.uk

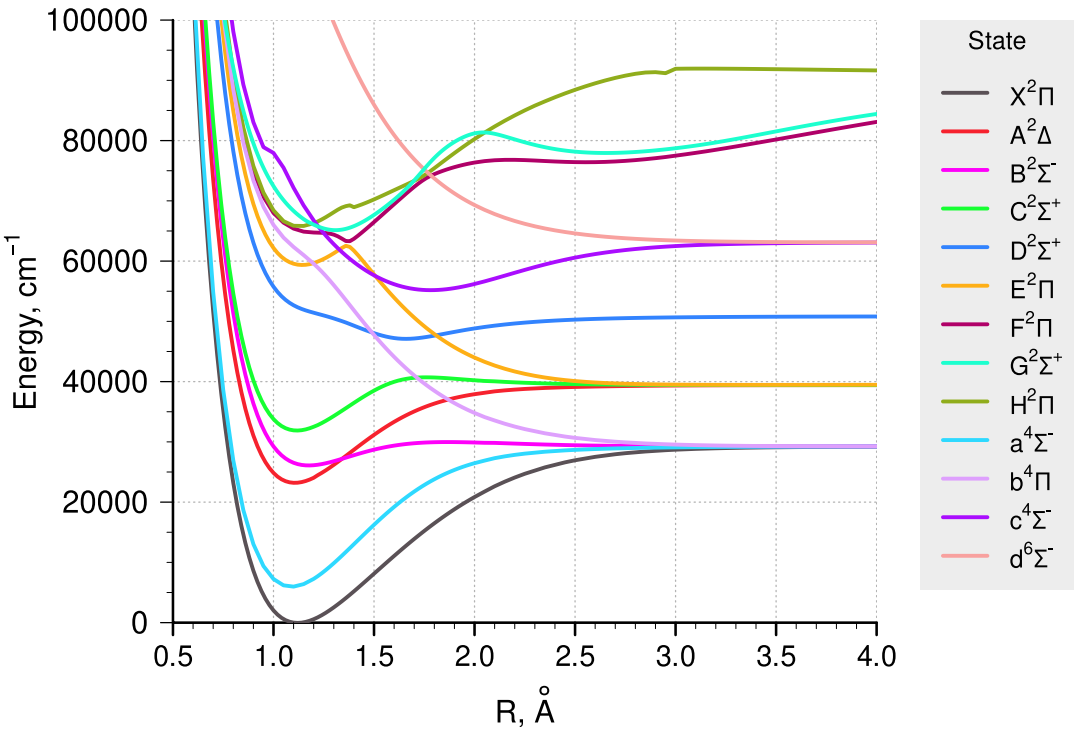

Figure 1. Potential energy curves for the states considered in this work.

2 METHODS

The model employed here was presented in detail by Sokolov, Yurchenko & Tennyson (2025). Below we summarize this model and consider details which extend the treatment from the one presented in our initial study.

2.1 Electronic structure data

Our spectroscopic model of CH consists of potential energy curves (PECs; see Fig. 1), permanent and transition dipole moments (TDM), and various electronic couplings which come mainly from a recent work by Hou & Liu (2024), with some data taken from Brady (2025) and van Dishoeck (1987). The potentials of the six lowest states were slightly adjusted as to ensure they go exactly to their respective dissociation asymptotes. The left well of the G $^2\Sigma^+$ state has been shifted down by 2902.9 cm^{-1} to improve agreement with theoretical dissociation energy D_e values (Kalemos, Mavridis & Metropoulos 1999; Vázquez et al. 2007) and also bringing the *G–X* band to lower frequencies as suggested by the experiment (Herzberg & Johns 1969). The treatment of non-adiabatic couplings among $^2\Sigma^+$ states and among $^2\Pi$ states is described in Appendix A.

2.2 Nuclear motion calculations

The Shrödinger equation for the set of coupled electronic states is solved variationally using the open-source code DUO by Yurchenko et al. (2016). Originally designed to treat bound state problems, it can also produce a discretized representation of unbound states above the dissociation limit as solution of a particle in box problem. In our methodology, associated transitions to and from these discrete states are used to produce photodissociation and photoabsorption spectra using a Gaussian-smoothing approach as described in detail by Pezzella et al. (2021), Mitev et al. (2025), and Uhlíková et al. (2025).

For the set of electronic structure data selected for our spectroscopic model, the DUO calculation produces a complete line list for CH, and we obtain theoretical, temperature dependent spectra that are representative up to 100 000 cm^{-1} at low temperatures and roughly 70 000 cm^{-1} at higher temperatures, where the lower levels of radiative transitions belong to excited electronic states. This is illustrated by the partition function shown in Fig. 2. Up to 3000 K, one only needs to consider the ground electronic state. At higher temperatures, the lowest quartet state a $^4\Sigma^-$ starts to get populated, and as shown in the inset, above 4000 K the total partition function starts to deviate again as more and more highly excited states (i.e. A $^2\Delta$, B $^2\Sigma^-$) get populated. These are compared to the partition function by Barklem & Collet (2016) as well as to the MoLLIST partition function of CH as provided computed by ExoMol (Wang, Tennyson & Yurchenko 2020).For comparison purposes, the former is multiplied by $g_{\rm nucl}$ to conform to the HITRAN convention (Gamache et al. 2025) used by ExoMol. The MoLLIST partition function was constructed by summation of states from the MoLLIST (Bernath 2020) CH line list over levels up to 500 K and then patched with the values obtained using Sauval & Tatum (1984). The agreement among data sets is good up to 4000 K. Above this temperature, the partition function from this work is larger due to a more complete spectroscopic model.

2.3 Bound and unbound solutions

Photodissociation can occur as a result of several different processes (Herzberg 1939; Schinke 1993; Heays et al. 2017). One

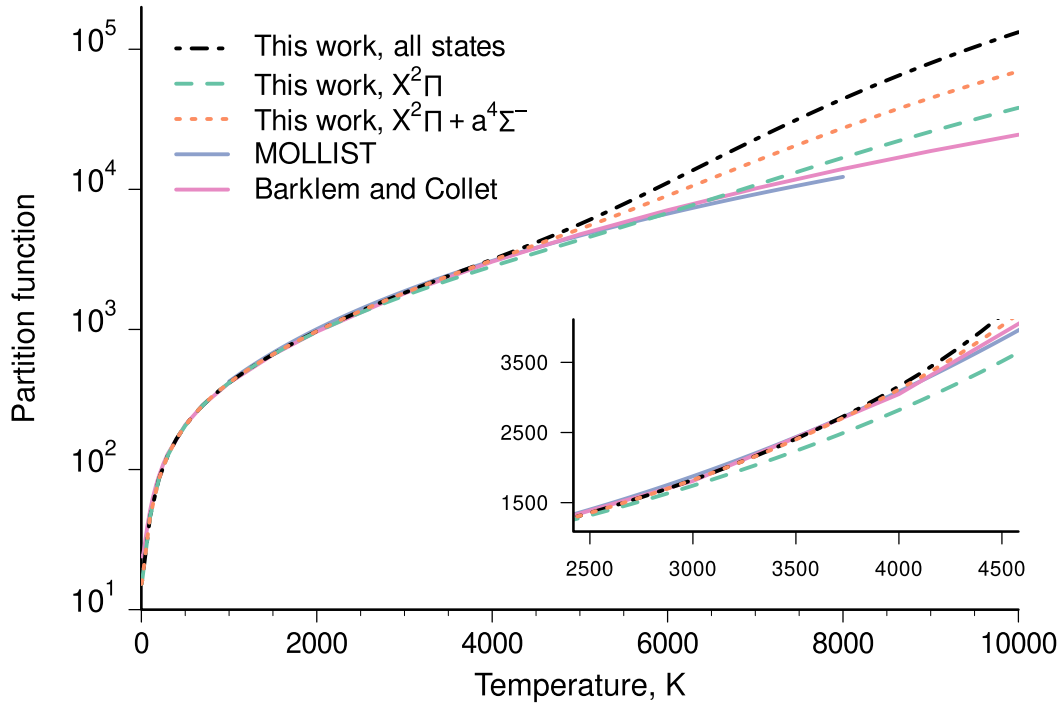

Figure 2. Comparison of partition functions calculated in this work, Masseron et al. (2014) and Barklem & Collet (2016). The inset shows the region where incompleteness of input states becomes noticeable.

of them is direct photodissociation, where the radiative transition happens between bound and continuum states. Another one is predissociation, a two-step process where absorption transfers the molecule into a quasi-bound (predissociative) state with the lifetime $\tau_{\rm total}$ that can either dissociate with efficiency $\eta = k_{\rm pred}/k_{\rm total} = (1/\tau_{\rm pred})/(1/\tau_{\rm total})$ or experience other radiative transitions. Here, $\tau_{\rm pred}$ and $\tau_{\rm total}$ are the lifetime due to the predissociation only and the total lifetime, respectively, and $k_{\rm pred}$ and $k_{\rm total}$ are the corresponding photodissociation rates. Direct photodissociation leads to broad uniform spectral features, while the predissociation spectrum consists of individual lines with width depending on the lifetimes of those quasi-bound states and are defined by the shapes and relative positions of the potential energy curves involved in the predissociation, as well as couplings between those electronic states.

We wish to distinguish more thoroughly between quasi-bound and unbound solutions of DUO. The default approach used by the code is to check the presence of a long oscillating tale in the (ro)vibronic probability distribution given in terms of the wavefunction by $|\psi_i|^2$ which is characteristic for unbound states. However, this approach often fails for quasi-bound states that also exhibit this feature while being much more localized around the potential well minimum. A more robust approach that we use here is to calculate the expectation value of the bond length $\langle r_{\rm CH}\rangle$ in a given state ψ_i or some similar quantity (Császár et al. 2020) which remains smaller for resonance states than for unbound ones. The distribution of $\langle r_{\rm CH}\rangle$ values for various selected states is shown in Fig. 3. The bound states, characterized by smaller values of $\langle r_{\rm CH}\rangle$, are located inside their respective potential energy wells, whereas the unbound states in our approach are located roughly the middle of the simulation box, between the right boundary and the repulsive wall of the respective PECs, $\langle r_{\rm CH}\rangle \sim 3.5$ Å. The quasi-bound states form the intermediate group between these two limits. To proceed with the calculation of dissociation rates, we draw the boundary at $\langle r_{\rm CH}\rangle = 3$ Å and label the states as bound or unbound in DUO's .states files. This single criterion works well for the low-lying states ($c\,^4\Sigma^-$ and below) with few couplings, where temperature dependence of rates would show up the strongest. For highly excited electronic states, a simple criterion is no longer sufficient. The potential energy wells of Rydberg-like states become wide (i.e. $G\,^2\Sigma^+$, $F\,^2\Pi$), so their levels or levels strongly coupled to such states require much larger box sizes or state-dependent cut-off values.

2.4 Direct photoabsorption

Using the procedure outlined in the previous section, we use DUO to compute a bound–free line list represented by transitions from bound to discretized unbound states, which is then used to produce temperature-dependent bound-free cross-sections using the ExoCross programme (Yurchenko, Al-Refaie & Tennyson 2018). Here, the associated discrete lines are smoothed using the particle-in-a-box analogy of Uhlíková et al. (2025), where each line is broadened by a Gaussian whose width is given as a function of the v quantum number. The continuum absorption spectrum and the initial discrete 'stick' spectrum for transitions from $X\,^2\Pi$ state to various excited states are shown in Fig. 4. Our procedure appear to produce sensible spectral shapes, with a sharp and correct boundary for the dissociation limit, smooth broad features at lower frequencies and no oscillations in semilog scale due to underbroadening for large v. At higher frequencies, the theoretical spectrum starts to look more jagged due to shortcomings of our quasi-bound state classification, where more and more of quasi-bound states end up identified with the continuum.

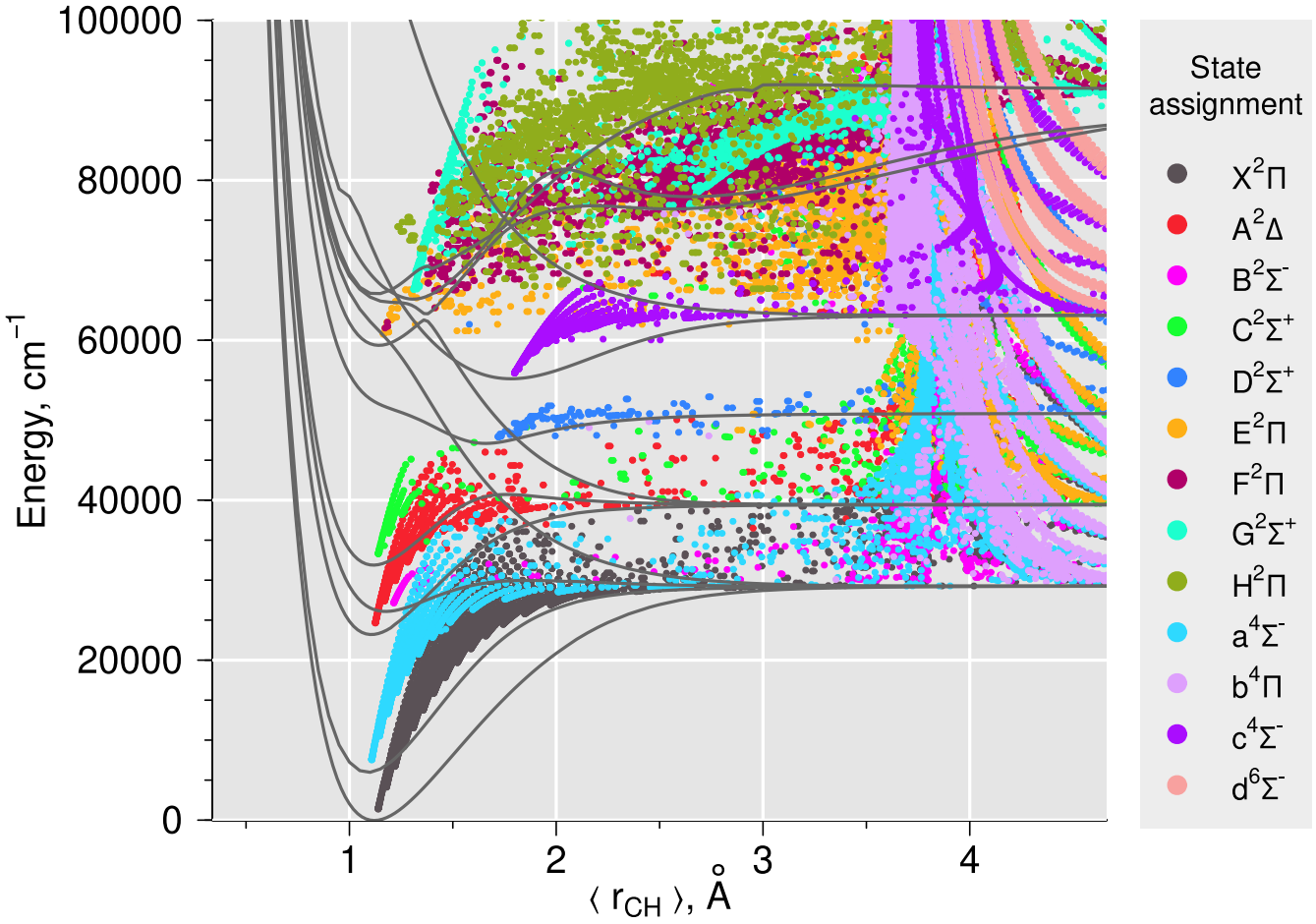

Figure 3. Diagram of the C–H bond length expectation values showing the distribution of selected rovibronic states ψ_i as energies versus associated $\langle r_{CH} \rangle$ values. These $\langle r_{CH} \rangle$ values were used in distinguishing unbound and (quasi-)bound states. Only some states with $\langle r_{CH} \rangle$ >4 Å are plotted to reduce clutter.

To further benchmark our time-independent approach against the scattering formalism, we compared the cross-sections by van Dishoeck (1987) to our photoabsorption calculations using their PECs and TDMs for the *B*–*X* and *D*–*X* bands as shown in Fig. 5. For the case of the *B*–*X* band, the agreement between the methods is reasonable. Two differences stand out, the peak in the shaded predissociative region and the intensity discrepancy at higher frequencies. The peak appears due to the presence of predissociative upper states in the *B*–*X* (1,0) band, and the $\langle r_{CH} \rangle$ filter helps move most of it (red versus blue lines) into the bound-quasi-bound part of the problem, leaving only upper states with $\langle r_{CH} \rangle > 4.3$ Å in the blue contribution. As for the intensity in high frequency wing, it might be overestimated because the v quantum numbers of the upper unbound states are relatively low, so transitions to those very first states get overbroadened, see Uhlíková et al. (2025, Fig. 6). For the *D*–*X* band, the Franck–Condon factors favour transitions to states with high v where the particle-in-a-box approximation works well, and the agreement with scattering calculations is excellent.

2.5 Predissociative transitions

From a theoretical point of view, several kinds of predissociative processes are possible in diatomic molecules (Herzberg 1939). Relevant to this work are Type I and Type III. Type I is the predissociation due to coupling to the continuum, where a bound state gets some unbound character from a dissociative curve; in this case predissociation depends on how strong the couplings are (Fano 1961). Type III is predissociation by rotation, where a state with energy above the dissociation limit can tunnel through the centrifugal barrier and reach the continuum. Type I process can occur for any state above the dissociation limit. Type III process, in turn, requires a rotational barrier and is relevant for rotationally excited states that are usually inaccessible by single photon absorption in cold media. As this study also concerns hot environments, we include both mechanisms in the model.

Experimentally, predissociation in absorption spectra is often observed as diffuseness and broadening of spectral lines beyond that which can be expected from other broadening mechanisms. Thus, accurate low-pressure experiments can provide the width of a transition and the total lifetime of the upper state τ_{total} (assuming the lower state is bound). Theory, in turn, helps to obtain radiative lifetimes from the knowledge of the Einstein A-coefficients $\tau_{rad} = 1/\sum_f A_{fi}$, as well as predissociative lifetimes τ_{pred}.

The Einstein coefficients and the radiative lifetimes are obtained as a part of the solution by DUO. Type I predissociation is treated here using the stabilization approach (Hazi & Taylor 1970; Mandelshtam, Ravuri & Taylor 1993; Mitev et al. 2025); a detailed study of it has been reported separately (Sokolov et al.

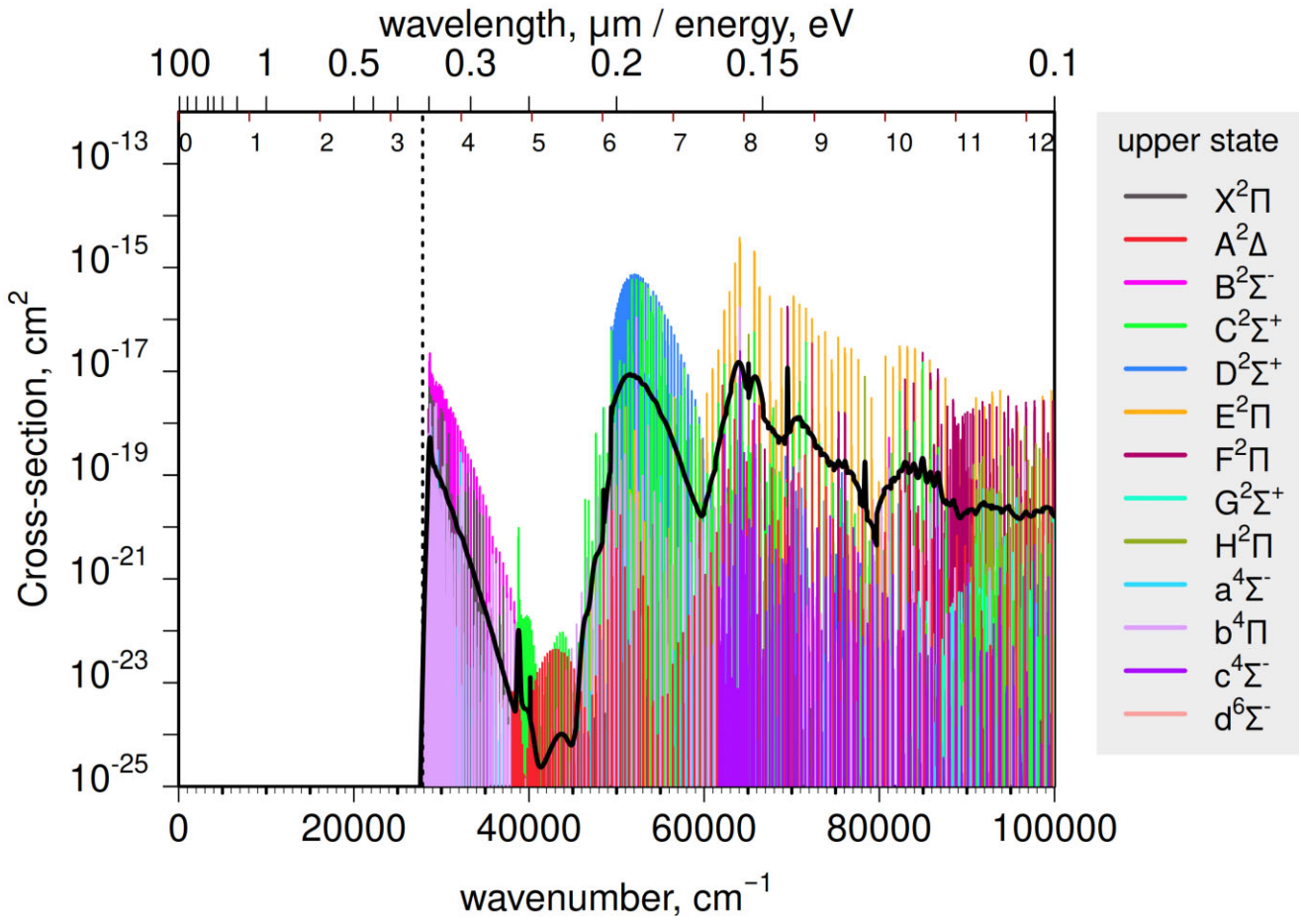

Figure 4. Continuum absorption cross-sections at 1 K using the particle-in-a-box broadening (black solid line) and the initial discrete 'stick' spectra. The dashed line represents the threshold to photodissociation, D_0.

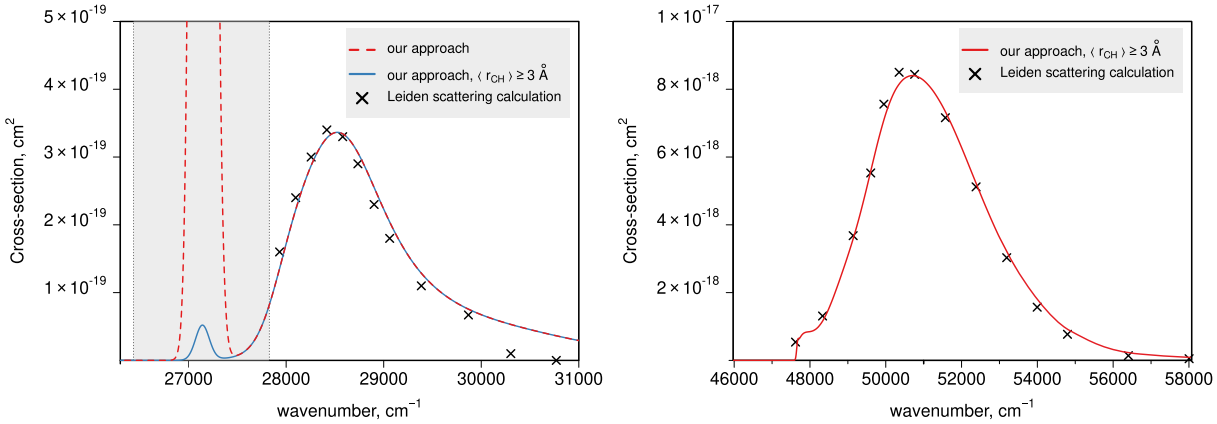

Figure 5. Comparison of direct photoabsorption *B*–*X* (left) and *D*–*X* (right) features calculated by van Dishoeck (1987) using the scattering approach and this work using the same set of PECs and TDMs at 1 K. The shaded region corresponds to the quasi-bound states.

2025). Briefly, by changing $L_{\max}$ in the DUO input, we monitor the change in the energy of predissociative states, and the widths of the resulting energy distributions are used to get the rates, $k_{\text{Type I}}$, and lifetimes.

Rotational predissociation lifetimes are computed using the code LEVEL (Le Roy 2017) which explicitly allows for the continuum using the semiclassical WKB (Wentzel-Kramers-Brillouin) approximation to calculate resonance widths (Le Roy & Bernstein 1971; Huang & Le Roy 2003). Given a PEC for an isolated electronic state, LEVEL provides resonance widths for each (quasi-)bound rovibrational state i, which are then converted to predissociative lifetimes $\tau_{\text{Type III}} = \gamma^{\text{FW}}/(2\pi c)$. The assignment of rotational quantum numbers N and

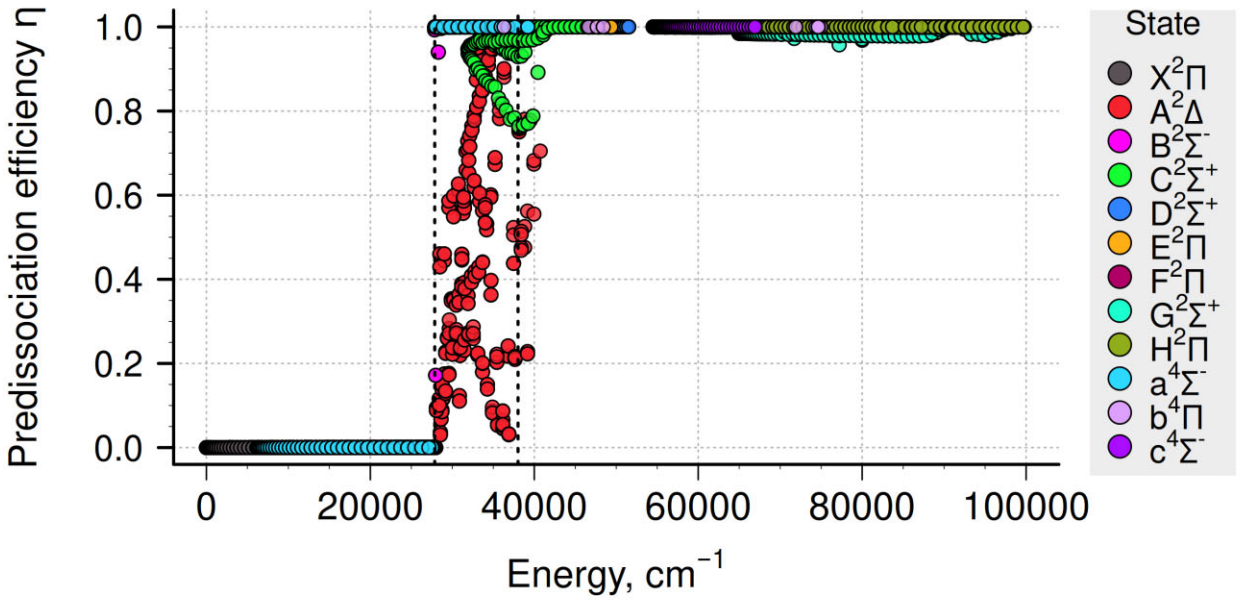

Figure 6. Predissociation efficiency for various rovibronic states of CH. Dashed lines mark the first and second dissociation thresholds.

F_i to the DUO results that are needed for merging with LEVEL output were performed following the conventions of Whiting (1973).

To reiterate, we aim to produce photodissociation cross-sections to be used in production of photodissociation rates. As discussed above, we construct these cross-sections from two main contributions (see Mitev et al. 2025): (1) cross-sections computed from the bound–free transitions and (2) cross-sections computed from bound–quasi-bound transitions. While the bound–free cross-sections are obtained directly from a discretized line list using the Gaussian-smoothing procedure (see above), the quasi-bound cross-sections are generated from the bound–bound line list using a proper lifetime broadening mechanism. To this end, we need assess whether a transition to an excited state is predissociative as opposed to truly bound, and if so, how efficient the dissociation process is. In this work, we neglect collisional effects and consider the predissociation efficiency η as a fraction of the predissociation rate $k_{\rm pred}$ to the total rate $k_{\rm total}$:

$$\eta = k_{\rm pred}/k_{\rm total}, \tag{1}$$

where

$$k_{\rm total} = k_{\rm rad} + k_{\rm pred} = \frac{1}{\tau_{\rm rad}} + \frac{1}{\tau_{\rm pred}}. \tag{2}$$

If both Type I and III mechanisms contribute to the predissociation, their rates are added, i.e. $k_{\rm pred} = k_{\rm Type\,I} + k_{\rm Type\,III}$. We then modify the Einstein A coefficients computed by DUO in.trans file by scaling them with the predissociation efficiency η as

$$\tilde{A}_{fi} = \eta_f A_{fi}. \tag{3}$$

Since η represents the quasi-continuum portion of the photoabsorption, this expression allows to properly account for the quasi-continuum contributions to photodissociation. Indeed, for the pure bound–bound states, $\tau_{\rm pred} = 0$ and $\eta = 0$ and therefore the corresponding contribution to photodissociation will be zero as well. We also modify the .states file by replacing the state radiative lifetimes $\tau_{\rm rad}$ with the total lifetimes $\tau_{\rm total} = k^{-1}_{\rm total}$, which is then used in line broadening.

In this work, predissociation was considered in detail only for a few low-lying electronic states, and predissociation efficiency is illustrated in Fig. 6. For states B $^2\Sigma^-$, a $^4\Sigma^-$, and X $^2\Pi$, only Type III process is possible, and these were treated with LEVEL. Transitions to the B-state are by far the most important ones in this group, as the spin-forbidden a–X radiative transitions have not, to the best of our knowledge, been observed, while transitions within the ground electronic state with large Δv are weak. At $T = 0$ K, transitions to predissociating rotational levels with high J do not occur due to low populations of the appropriate $J_{\rm lower}$, and this mechanism is irrelevant for extremely cold media. However, for objects with higher temperature, these rotational states can become populated, and above 3000 K the contribution to the partition function even from the a $^4\Sigma^-$ state is not negligible.

Electronic states A $^2\Delta$ and C $^2\Sigma^+$ tend to the second dissociation limit. For them, both Type I and III processes have been considered, and numerous rovibrational levels are affected by predissociation effects. The A $^2\Delta$ state supports nine vibrational states, and we observe different behaviour of η for levels with different v, $|\Omega|$, J shown in red. In the C $^2\Sigma^+$ state, η shows different behaviour for groups with different v, J, and parity, and one can see a long-living component with decreasing predissociation rate for the $v = 0$ state in bright green.

For the G $^2\Sigma^+$ state, η is obtained from our radiative lifetimes and $k_{\rm Type\,I}$ is estimated from van Dishoeck (1987). Although our spontaneous radiative rates $k_{\rm rad} \sim 1.2 \times 10^8$ s^{-1} are twice as high as previously reported, the lower limit for the predissociation rate $k_{\rm pred} = 7.6 \times 10^9$ s^{-1} is still ~ 60 times larger and these states predissociate almost completely (cyan points in Fig. 6).

Such (almost) complete predissociation of bound levels is a general feature of highly excited electronic states with a lot of couplings and a dense continuum of lower lying states. Li & Lee (1999) extracted experimental lifetimes for D $^2\Sigma^+$, $v = 0$ states from absorption

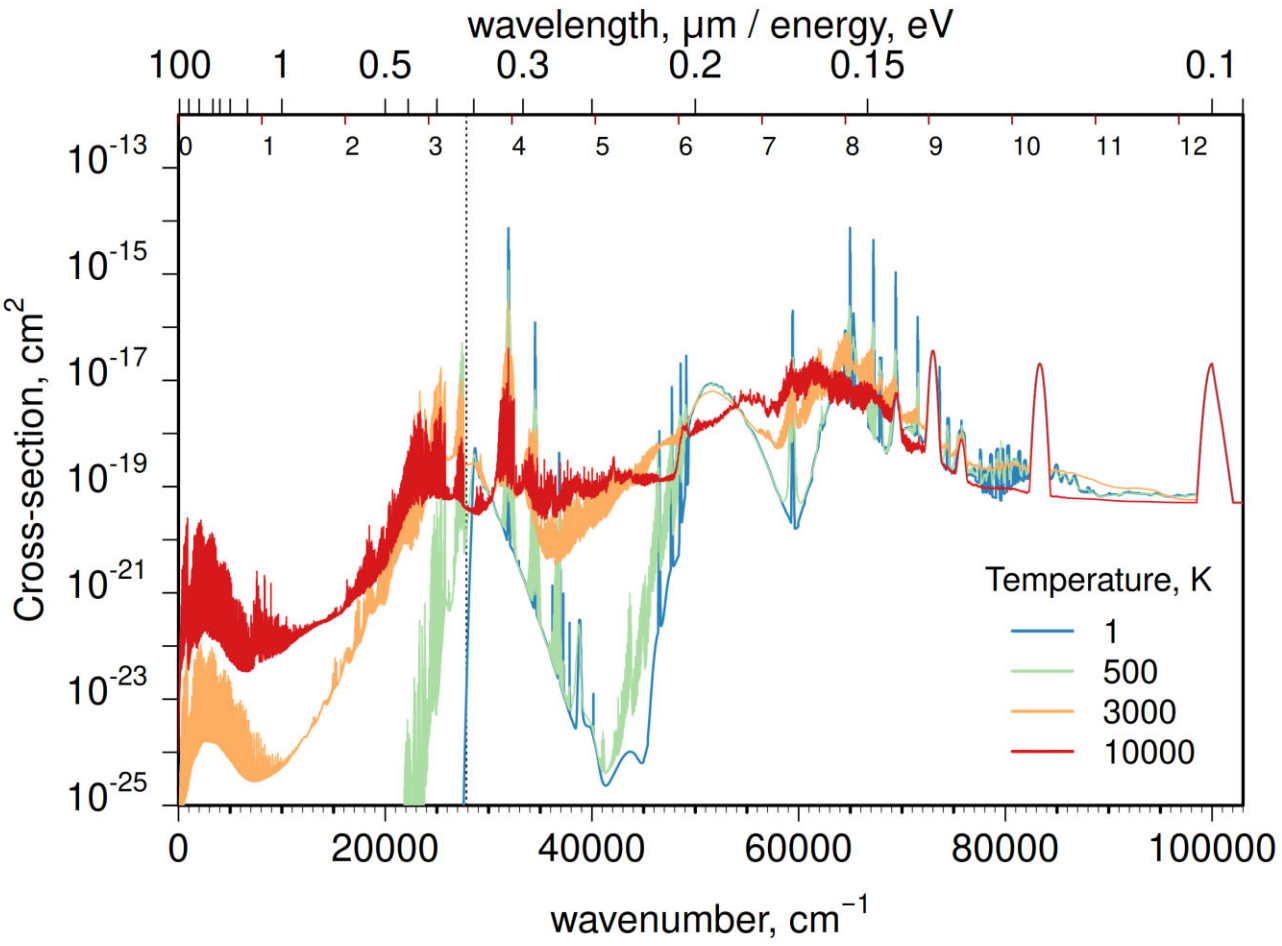

Figure 7. Photodissociation cross-sections at different temperatures with a temperature-independent short wavelength top-up. The dashed line marks D_0, below which photodissociation at 0 K is not possible. The figure contains multiple frequency/wavelength axis scales (cm^{-1}, μm, and eV) for convenience.

spectra measurements and obtained values of the order of $\tau_{expt} \sim 1$ ps compared to our $\tau_{rad} > 100$ ns. The discrepancy must be attributed to predissociation which happens with almost 100 per cent efficiency. The reduction of lifetime also leads to broadening, and these lines have halfwidths over 2 cm^{-1}. DUO predicts four bound vibrational states in $D\,^2\Sigma^+$ electronic state, but in the experiment the lines with the upper $v = 1$ state are so broad they are not observed at all (Herzberg & Johns 1969; Li & Lee 1999). Metropoulos & Mavridis (2000) calculate τ_{pred} for $E\,^2\Pi$, $v = 0, 1, 2$, and $F\,^2\Pi$ $v = 0, 1, 2$ which range from 2 ps to 2 fs. Our radiative lifetimes for these do not fall below 2 ns, and again $\eta \approx 1$. Data are not available for the two remaining bound electronic states in our set, $H\,^2\Pi$ and $c\,^4\Sigma^-$. The $H\,^2\Pi$ state is strongly coupled to $E\,^2\Pi$ and $F\,^2\Pi$, both with short τ_{pred}, so we set $\tau_{pred} = 1$ fs for $H\,^2\Pi$. As for the quartet state, it crosses a number of curves where the spin-orbit coupling is small, but not zero, and here we also assumed a short lifetime of 1 fs and $\eta = 1$.

To calculate the cross-sections, we modify the Einstein coefficient of each predissociative transition by predissociative efficiency as discussed above. Each line is also broadened with the Voigt profile, where the Lorentzian component comes from the total lifetime, and the Doppler component uses the temperature of the gas. A 100 cm^{-1} cut-off is used to truncate the line wings, and to conserve the intensity, we transfer the same amount of intensity from the wings into the 'pedestal' of the line. Note that for $\tau = 1$ ps, the half-width is $\gamma = 2.65$ cm^{-1}, and such a cut-off is adequate, but for shorter lifetimes, i.e. $\tau = 5$ fs, $\gamma = 530$ cm^{-1}. This means that a significant portion of the line wings for lines above ~ 5 eV gets folded back, and a feature that would appear broad instead looks sharp. Using a larger cut-off negatively affects the lines at lower frequencies, where the slowly decaying wings can spread beyond the wavelength, corresponding to D_0.

2.6 Short wavelength top-up

Despite a large number of PECs and TDMs used in this work, some data for the higher electronic states of CH are still missing. van Dishoeck (1987) discusses the contributions from absorption into the $4\,^2\Sigma^+$ state at 8.6 eV, the three states constituting the $3d$ Rydberg complex, $2\,^2\Delta$, $5\,^2\Pi$, $5\,^2\Sigma^+$, at around 9 eV (Vázquez et al. 2007), and the $3\,^2\Delta$ state at 9.4 eV. Absorption into those states always leads to molecular dissociation. Also mentioned are the higher lying doublet states of Rydberg character that converge to the first ionization threshold (10.64 eV) and those states of the neutral CH radical that converge to the excited states of the CH^+ ion, $a\,^3\Pi$, and $A\,^1\Pi$ (Chakrabarti, Ghosh & Choudhury 2019). In this region, dissociation starts to compete with ionization of the

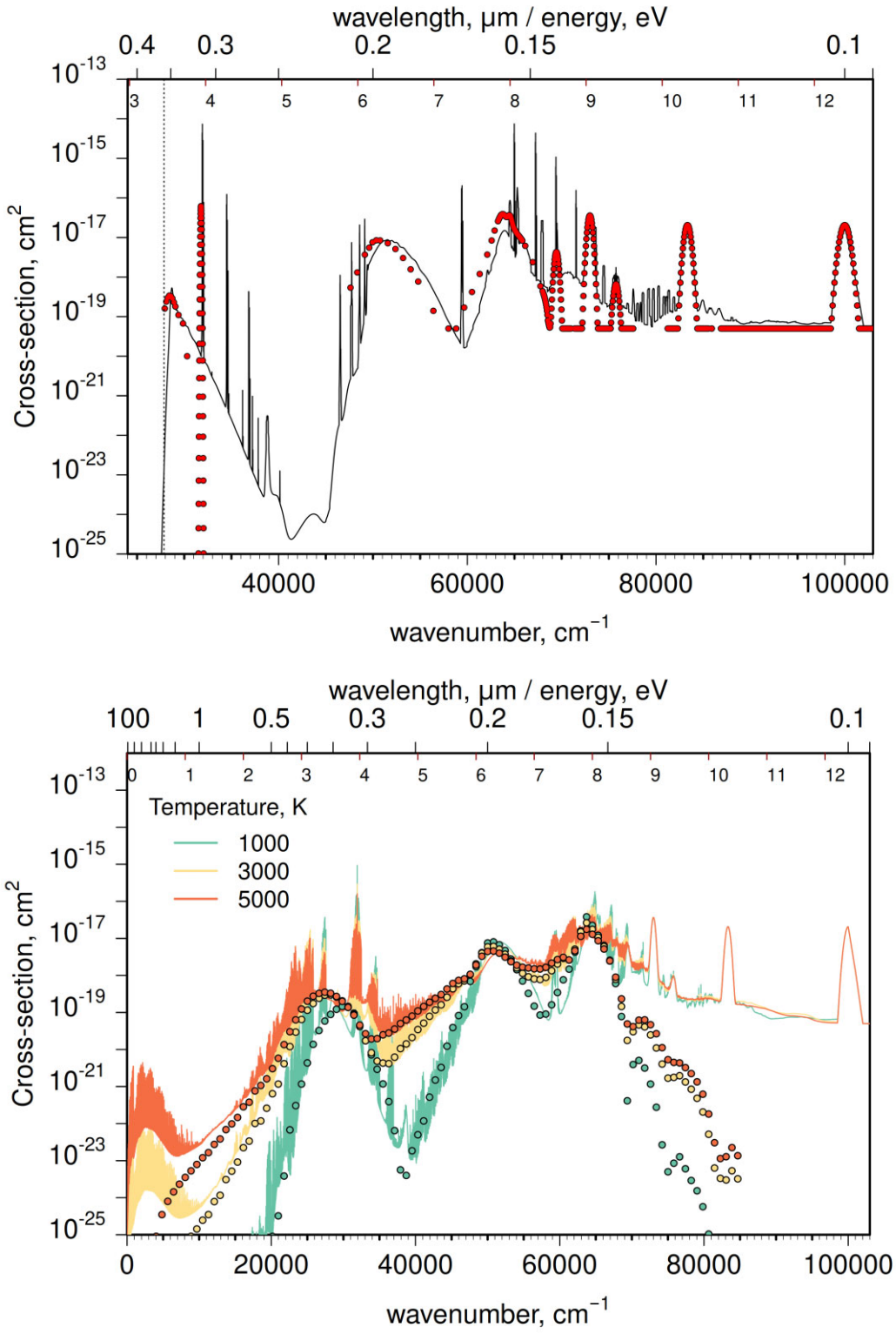

Figure 8. Comparison of photodissociation cross-sections from this work with the literature data. Top: comparison of 1 K cross-section with the Leiden data base (Hrodmarsson & Van Dishoeck 2023). Bottom: comparison with Kurucz et al. (1987) for high temperatures.

molecule and the photodissociation rate quickly goes down. We use these estimates from the Leiden data base (van Dishoeck 1987) as a short-wavelength top-up without any changes and do not include the temperature dependence of cross-sections or rates coming from transitions to these states. The integral of the photodissociation cross-sections for those bands beyond 8.5 eV is 6.18×10^{-14} cm, which is roughly a third of the entire cross-section given by Leiden.

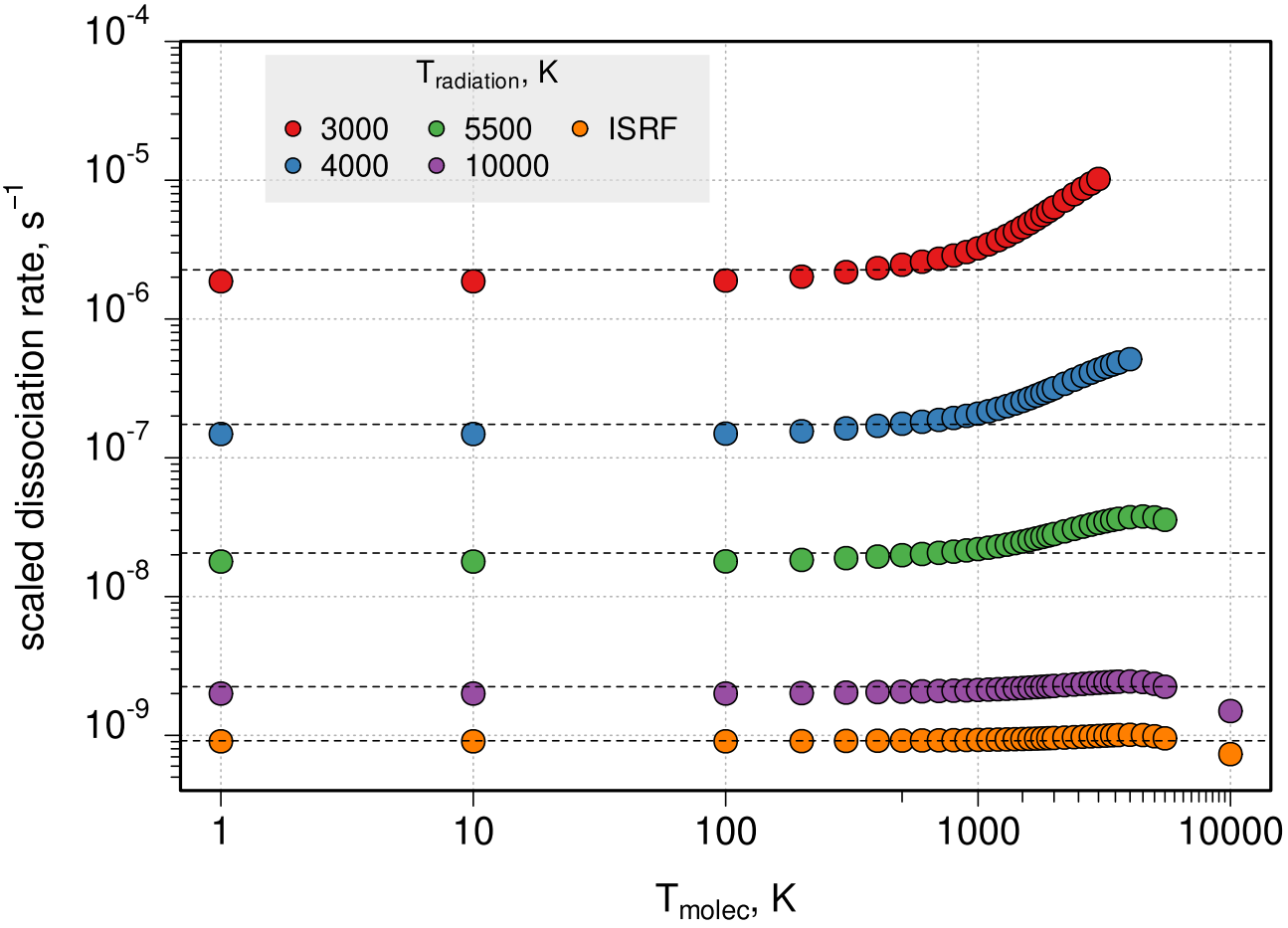

Figure 9. Photodissociation rates for various gas temperatures and radiation fields (four blackbody fields for different radiation field temperatures and the interstellar radiation field). Horizontal lines are 0 K rates from Leiden. For each radiation field, the rates are scaled according to Hrodmarsson & Van Dishoeck (2023).

2.7 Photodissociation cross-sections and rates

The photodissociation cross-section is that part of the (total) photoabsorption cross-section that contributes to the process of molecular break-up into neutral fragments. Here, we provide photodissociation cross-sections per molecule calculated from the DUO outputs using ExoCross on 0.1 nm grid for 34 temperatures (Pezzella, Tennyson & Yurchenko 2022). The current data set, named SBYT after the names of the present authors, is provided in the standard ExoMol format (Ni et al. 2025). Fig. 7 shows the temperature-dependence of these cross-sections against frequency; wavelength and energy units are also shown for convenience. We can see that for low gas temperatures, there is a clear threshold for the (UV) photon energy needed to induce photodissociation, marked by the dashed line. As the temperature increases, more and more excited rovibronic levels become populated. Because of this, the photon energy needed to reach the quasi-bound levels of CH drops, and so the threshold shifts towards lower frequencies. It is this behaviour of the cross-sections that is responsible for temperature dependence of photodissociation rates in radiation fields which peak at long wavelengths.

Fig. 8 compares our cross-sections with the literature data. The first panel shows comparison with the Leiden data base for cold temperatures. This work shows more numerous, rovibrationally resolved sharp predissociation features. Compared to Leiden, the positions of some lower energy features are shifted due to the different set of potential energy curves and couplings used here. The second panel shows that the overall shape of high-temperature continuum absorption cross-sections of Kurucz et al. (1987) is very close to ours. However, our new data include predissociation effects and more electronic states not considered by Kurucz et al. (1987), which explains the differences at both low and high frequencies, respectively.

The photodissociation rates (s^{-1} molecule^{-1}) are computed as

$$k(T) = \int F(\lambda)\sigma(\lambda;T)\mathrm{d}\lambda, \tag{4}$$

where $\sigma(\lambda)$ are the wavelength-dependent photodissociation cross-sections and $F(\lambda)$ is the spectral irradiance per unit wavelength for various light sources. The expression for blackbody radiation (photons s^{-1} cm^{-2} nm^{-1}) is given by

$$B_\lambda^N = \frac{8\pi c}{10^{13}\cdot\lambda^4}\frac{1}{\exp\left[hc/(\lambda kT)\right]-1}, \tag{5}$$

where all the input quantities are in SI. The expression for the interstellar radiation field (ISRF) is taken from Hrodmarsson & Van Dishoeck (2023). The rates in this work are computed with the Leiden convention (Heays et al. 2017; Hrodmarsson & Van Dishoeck 2023), where the irradiance for each light source is renormalized such that the energy density between 91.2 and 200 nm is equal to that of the Draine field. The actual dissociation rates in the blackbody field increase drastically with radiation temperature, while the opposite is observed when the flux is renormalized.

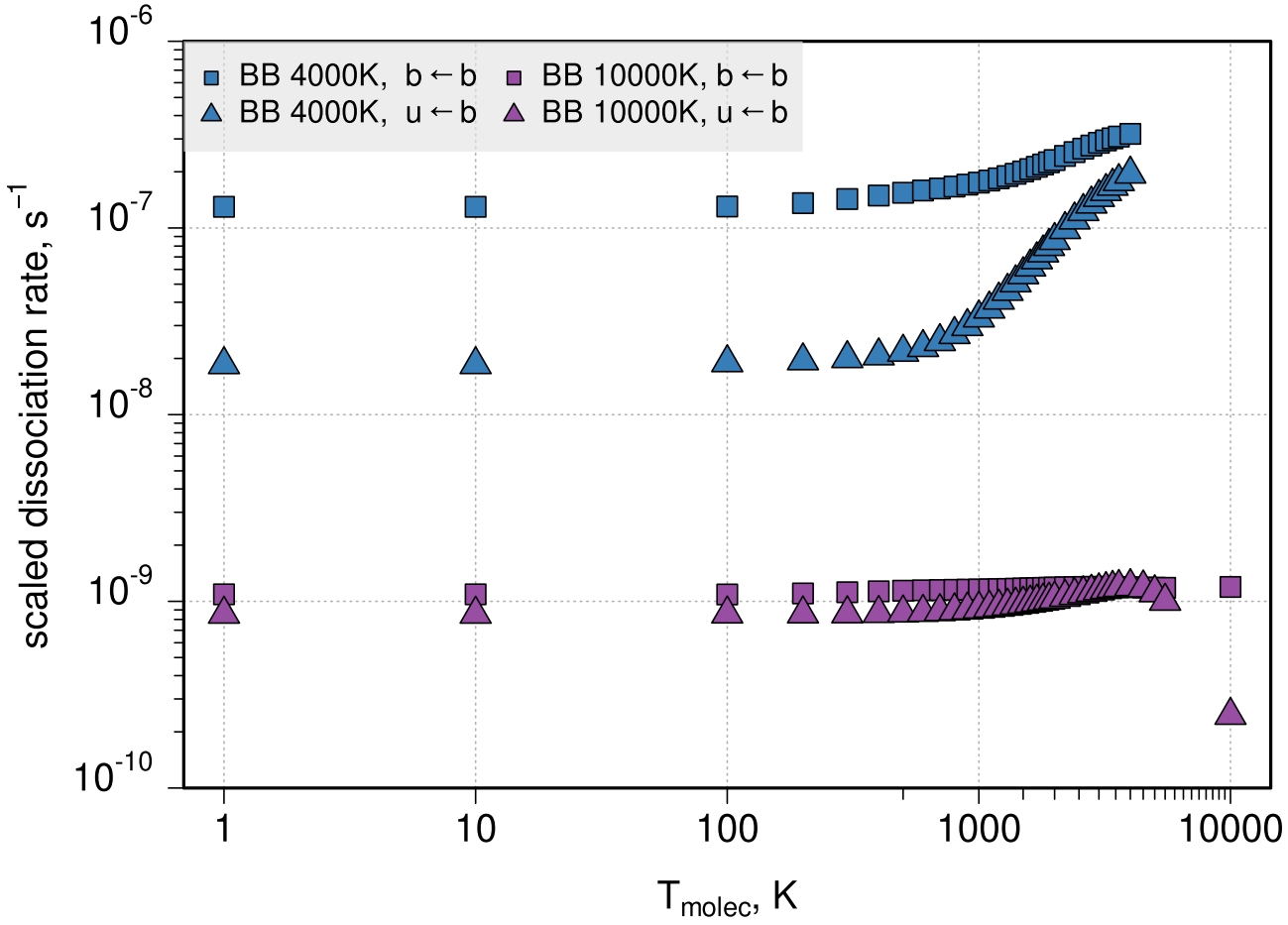

Figure 10. Contributions to photodissociation rates from predissociation (bound–bound transitions) and direct photoabsorption (bound–unbound transitions) for two radiation fields.

Fig. 9 shows the temperature dependence of the CH photodissociation rates for various light sources. Dashed horizontal lines represent the (temperature-independent) values from the Leiden data base obtained by integrating their low temperature cross-sections with the appropriate flux. These data agree very well with our calculations at 1 K, differing for BB4k (blackbody at 4000 K), BB10k, and ISRF by 0.86, 0.91, and 0.99, respectively. The cross-section top-up has no affect for BB4k rates, but increases the BB10k and ISRF rates by 3 per cent and 22 per cent, respectively. This shows the importance of considering the highly excited electronic states in extremely UV-rich environments, but for low-temperature stars the contribution to photodissociation from those high-frequency transitions will be negligible.

As for the effect of gas temperature, weak dependence is observed for those rates where the flux has a flat spectral profile across the region of molecular absorption, i.e. for ISRF and BB10k. For lower temperature radiation fields, the effect of gas temperature on rates is much more pronounced peaking for BB3k, where the difference in rates reaches $k_{\rm BB3k}(3000\ {\rm K})/k_{\rm BB3k}(1\ {\rm K}) \approx 5.5$ times. As cooler stars usually have higher CH abundance (Kurucz et al. 1987), the temperature dependence of these rates will have a stronger impact on their opacities. Fig. 10 shows contributions to our photodissociation rates (calculated without the cross-section top-up) from predissociation (squares) and direct photoabsorption (triangles) for 4000 and 10 000 K BB fluxes. The largest contribution in both cases comes from predissociation of quasi-bound states, while bound–unbound transitions are more sensitive to temperature effects.

Overall, the effect of the gas temperature on the rates for CH is much less extreme than that obtained for other hydrides. OH shows an order of magnitude increase for ISRF and four orders difference for BB4k rates (Mitev et al. 2025). This appears to result from a single large bound-free spectral feature that shifts from $\sim$ 200 nm to longer wavelengths as the temperature increases. A similar change is obtained for HF by Pezzella et al. (2022), while a more mild change of about a factor of 100 in $k_{\rm BB4k}$ rates is obtained for HCl. We believe this can be explained by the type and position of electronically excited states.The 1 K BB4k dissociation rates for CH, OH, HCl, and HF are, respectively, 1.5×10^{-7}, 2.8×10^{-10}, 9.4×10^{-11}, and 5.3×10^{-13} s^{-1}. This indicates a much higher dissociation rate for CH which, as shown on Fig. 10, comes mainly from predissociation. Indeed, CH has a number of electronic states that support quasi-bound levels in the energy range between 3.6 and 9 eV and only two states of the same multiplicity with a repulsive slope in the Franck–Condon region. The intensity of those B $^2\Sigma^-$ and D $^2\Sigma^+$ features is rather small compared to other bound–bound features (compare, for example, Fig. 7 with Mitev et al. 2025, Fig. 4). In contrast, within the same energy region OH has just a single bound state and three repulsive ones, while both HCl and HF have just a single repulsive state. As Fig. 10 shows, it is mainly the bound–free transitions that

are responsible for strong temperature dependence of dissociation rates.

Another curious feature in the present results is the drop in rates for high-energy flux distributions at high molecular temperatures. One of the reasons for this is the approximate, temperature-independent top-up for high-energy cross-sections. Another reason is the emerging competition between photodissociation and photoionization. We can expect a shift of the photoionization cross-sections to lower frequencies with temperature similar to the one we observe for molecular dissociation processes. Recently, Penson et al. (2025) studied the photoionization cross-sections of CH starting at $v = 0, 1, 2$ of the $X\,^2\Pi$ state and showed that the onset shifts from 10.62 to 10.1 eV when starting from higher v. Moreover, at 10 000 K the $a\,^4\Sigma^-$, $A\,^2\Delta$, and $B\,^2\Sigma^-$ states are sufficiently occupied, so even absorption of an 8 eV photon can cause a transition to the ionic states of CH^+. This hints at possible temperature effects of photoionization rates, and that including more electronic states beyond those already consider in the top-up is unlikely to lead to meaningful changes in dissociation rates of CH.

3 CONCLUSIONS

We present calculated photodissociation cross-section set for CH called SBYT. All the rovibronic states above the first dissociation limit have been considered in predissociation processes, with particular attention to $A\,^2\Delta$ and $C\,^2\Sigma^+$ states in the near-UV. We considered Type I mechanism in detail for $A\,^2\Delta$ and $C\,^2\Sigma^+$ states and roughly for the $G\,^2\Sigma^+$ state, and Type III mechanism for $X\,^2\Pi$, $A\,^2\Delta$, $B\,^2\Sigma^-$, $C\,^2\Sigma^+$, and $a\,^4\Sigma^-$ states. The rest of the rovibronic states are assumed to dissociate with 100 per cent efficiency based on the comparison of the total experimental and theoretical radiative lifetimes ($D\,^2\Sigma^+$, $E\,^2\Pi$, $F\,^2\Pi$) or on the energy values of those states and the strength of couplings ($c\,^4\Sigma^-$, $H\,^2\Pi$). Direct photoabsorption has been calculated from all bound and quasi-bound levels where TDM curves between the initial and final electronic states are available.

We find the effects of predissociation, largely neglected or treated more simplistically in previous studies, to be important but the dependence of the photodissociation rate on the gas temperature to be significantly weaker than found in our previous studies. Results of this study can be obtained from the ExoPhoto data base (Ni et al. 2025) at www.exomol.com/exophoto. The cross-sections presented in the ExoPhoto data base use the assumption that the CH molecule is in LTE. In practice, our calculations which are performed state-by-state. If needed, these state-resolved cross-sections can be used to create non-LTE photodissociation rates (Mitev et al. 2025). The set of state-resolved cross-section, which form a much larger data set then the temperature-dependent cross-sections provided by ExoPhoto, can be obtained from the authors on request.

This work is part of series of studies on the photoabsorption properties of CH. This spectroscopic model used here, but adjusted to experiment is currently being used to produce an accurate, temperature-dependent CH line list (Yurchenko et al. 2025) as part of the ExoMol project. An analysis of the competition between radiative and predissociative decay mechanisms in excited electronic states of CH radical is being published elsewhere (Sokolov et al. 2025). These studies give good agreement with extensive experimental measurement of the properties considered. As the current calculations are based on essentially the same CH spectroscopic model, these comparisons give us confidence in the reliability of the cross-sections we present.

ACKNOWLEDGEMENTS

This work was also supported by the European Research Council (ERC) under the European Union's Horizon 2020 research and innovation programme through Advance Grant number 883830 and STFC grants UKRI1183 and ST/Y001508/1. The work used the DiRAC Data Intensive service DIaL2.5 at the University of Leicester, managed by the University of Leicester Research Computing Service on behalf of the STFC DiRAC HPC Facility (www.dirac.ac.uk). The DiRAC service at Leicester was funded by BEIS, UKRI, and STFC capital funding and STFC operations grants. DiRAC is part of the UKRI Digital Research Infrastructure.

DATA AVAILABILITY

The supplementary materials contain DUO input files for bound and unbound line lists. The LTE Boltzmann-averaged temperature-dependent cross-sections for 34 gas temperatures (cm^2 $molecule^{-1}$ versus nm) are available via the ExoPhoto data base www.exomol.com/ExoPhoto. Non-LTE cross-sections can be made available on request.

REFERENCES

Barklem P. S., Collet R., 2016, A&A, 588, A96
Bernath P. F., 2020, J. Quant. Spectrosc. Radiat. Transf., 240, 106687
Brady R. P., 2025, J. Chem. Phys., 162, 174105
Brady R. P., Yurchenko S. N., 2025, J. Comput. Chem., 46, e70181
Brady R. P., Drury C., Yurchenko S. N., Tennyson J., 2024, J. Chem. Theory Comput., 20, 2127
Chakrabarti K., Ghosh R., Choudhury B. S., 2019, J. Phys. B: Atom. Mol. Opt. Phys., 52, 105205
Civiš S., Pastorek A., Ferus M., Yurchenko S. N., Boudjema N.-I., 2023, Molecules, 28, 3362
Császár A. G., Simkó I., Szidarovszky T., Groenenboom G. C., Karman T., van der Avoird A., 2020, Phys. Chem. Chem. Phys., 22, 15081
De Nijs A. J., Ubachs W., Bethlem H. L., 2012, Phys. Rev. A, 86, 032501
Fano U., 1961, Phys. Rev., 124, 1866
Furtenbacher T., Hegedus S. T., Tennyson J., Császár A. G., 2022, Phys. Chem. Chem. Phys., 24, 19287
Gamache R. R., Vispoel B., Tennyson J., Yurchenko S. N., Polyansky O. L., Gordon I. E., Hargreaves R. J., Huang X., 2025, J. Quant. Spectrosc. Radiat. Transf., 345, 109568
Grevesse N., Lambert D., Sauval A., van Dishoeck E., Farmer C., Norton R., 1991, A&A, 242, 488
Hazi A. U., Taylor H. S., 1970, Phys. Rev. A, 1, 1109
Heays A. N., Bosman A. D., van Dishoeck E. F., 2017, A&A, 602, A105
Herzberg G., 1939, Molecular Spectra and Molecular Structure, Vol. 1, Diatomic Molecules. Prentice-Hall, New York
Herzberg G., Johns J. W. C., 1969, ApJ, 158, 399
Hou Z., Liu L., 2024, Phys. Chem. Chem. Phys., 27, 367
Hrodmarsson H. R., Van Dishoeck E. F., 2023, A&A, 675, A25
Huang Y., Le Roy R. J., 2003, J. Chem. Phys., 119, 7398
Jørgensen U. G., Larsson M., Iwamae A., Yu B., 1996, A&A, 315, 204
Kalemos A., Mavridis A., Metropoulos A., 1999, J. Chem. Phys., 111, 9536
Kurucz R. L., Van Dishoeck E. F., Tarafdar S. P., 1987, AJ., 322, 992
Lambert D. L., Gustafsson B., Eriksson K., Hinkle K. H., 1986, ApJS, 62, 373
Le Roy R. J., 2017, J. Quant. Spectrosc. Radiat. Transf., 186, 167
Le Roy R. J., Bernstein R. B., 1971, J. Chem. Phys., 54, 5114
Li X., Lee Y.-P., 1999, J. Chem. Phys., 111, 4942
Lien D., 1984, ApJ, 284, 578
Liu X.-W. et al., 1997, MNRAS, 290, L71
Mandelshtam V. A., Ravuri T. R., Taylor H. S., 1993, Phys. Rev. Lett., 70, 1932
Masseron T. et al., 2014, A&A, 571, A47

Mélen F., Grevesse N., Sauval A., Farmer C., Norton R., Bredohl H., Dubois I., 1989, J. Mol. Spectrosc., 134, 305
Metropoulos A., Mavridis A., 2000, Chem. Phys. Lett., 331, 89
Mitev G. B., Pezzella M., Bowesman C. A., Zhang J., Yurchenko S. N., Tennyson J., 2025, MNRAS, 539, 3732
Ni Q.-H., Hill C., Yurchenko S. N., Pezzella M., Fateev A., Qin Z., Venot O., Tennyson J., 2025, RASTI, 4, rzaf020
Penson C. et al., 2025, Phys. Rev. A, 111, 013105
Perri A. N., Mitrushchenkov A. O., Yurchenko S. N., Tennyson J., 2025, J. Chem. Phys.
Pezzella M., Yurchenko S. N., Tennyson J., 2021, Phys. Chem. Chem. Phys., 23, 16390
Pezzella M., Tennyson J., Yurchenko S. N., 2022, MNRAS, 514, 4413
Popa S. A., Hoppe R., Bergemann M., Hansen C. J., Plez B., Beers T. C., 2023, A&A, 670, A25
Rensberger K. J., Dyer M. J., Copeland R. A., 1988, Appl. Opt., 27, 3679
Ridgway S. T., Carbon D. F., Hall D. N. B., Jewell J., 1984, ApJS, 54, 177
Sauval A. J., Tatum J. B., 1984, ApJS, 56, 193
Schinke R., 1993, Photodissociation Dynamics. Cambridge Univ. Press, Cambridge
Sokolov A., Yurchenko S. N., Tennyson J., 2025, Phys. Chem. Chem. Phys.
Stacey G. J., Lugten J. B., Genzel R., 1987, ApJ, 313, 859
Truppe S., Hendricks R., Tokunaga S., Hinds E., Tarbutt M., 2014, J. Mol. Spectrosc., 300, 70
Uhlíková T., Yurchenko S. N., Perri A. N., Tennyson J., Kim G.-S., 2025, J. Chem. Phys., 162, 144108
van Dishoeck E. F., 1987, J. Chem. Phys., 86, 196
Vázquez G. J., Amero J. M., Liebermann H. P., Buenker R. J., Lefebvre-Brion H., 2007, J. Chem. Phys., 126, 164302
Versailles P., Watson G. M., Lipardi A. C., Bergthorson J. M., 2016, Combust., 165, 109
Wang Y., Tennyson J., Yurchenko S. N., 2020, Atoms, 8, 7
Whiting E. E., 1973, Computer Program for Determining Rotational Line Intensity Factors for Diatomic Molecules. National Aeronautics and Space Administration, Washington, DC
Womack M., Lutz B. L., Wagner R. M., 1994, ApJ, 433, 886
Yurchenko S. N., Lodi L., Tennyson J., Stolyarov A. V., 2016, Comput. Phys. Commun., 202, 262
Yurchenko S. N., Al-Refaie A. F., Tennyson J., 2018, A&A, 614, A131
Yurchenko S. N., Wharton H., Brady R., Tennyson J., 2025, MNRAS

SUPPORTING INFORMATION

Supplementary data are available at *MNRAS* online.
Please note: Oxford University Press is not responsible for the content or functionality of any supporting materials supplied by the authors. Any queries (other than missing material) should be directed to the corresponding author for the article.

APPENDIX A: TREATMENT OF NON-ADIABATIC COUPLINGS

If electronic states of the same symmetry are present in the model, one also needs to consider non-adiabatic couplings (NAC) to describe the avoided crossings regions and improve the accuracy of nuclear motion calculations. The inclusion of NACs can considerably change the intensity distribution for transitions to the coupled states (Brady et al. 2024; Brady & Yurchenko 2025; Perri et al. 2025). van Dishoeck (1987) considers such radial nuclear couplings among the excited $^2\Pi$ states, as well as between $C\,^2\Sigma^+$ and $D\,^2\Sigma^+$ in their spectroscopic model. For the former group of states, NACs lead to emergence of complicated resonance structures within the broad photoabsorption features. Hou & Liu (2024) also consider NACs and diabatize their set of *ab initio* PECs using the property-based diabatization approach for the two state pairs $E\,^2\Pi$–$F\,^2\Pi$ and $F\,^2\Pi$–$H\,^2\Pi$. In our work, we use the *N*-state hybrid asymptotic property based diabatization (HyAP) algorithm (Brady 2025) to simultaneously couple multiple states of the same symmetry and apply it to the $\Lambda = 0$ states ($C\,^2\Sigma^+$, $D\,^2\Sigma^+$, $G\,^2\Sigma^+$), and to the $\Lambda = 1$ states ($E\,^2\Pi$, $F\,^2\Pi$, $H\,^2\Pi$). The NACs for the $^2\Sigma^+$ states are taken directly from Brady (2025) as the set of potentials for these states is not too dissimilar to Hou & Liu (2024). The PECs for the $^2\Pi$ states, however, significantly differ in their minima positions between van Dishoeck (1987) and Hou & Liu (2024), and the NACs themselves are much stronger. As a result of using HyAP, we therefore regularize the NACs using *ab initio* NACs from van Dishoeck (1987) as starting estimates together with PECs from Hou & Liu (2024) to ensure smooth diabats for the coupled states.

This paper has been typeset from a TEX/LATEX file prepared by the author.